THE JOURNAL OF PHYSICAL CHEMISTRY C
A JOURNAL OF THE AMERICAN CHEMICAL SOCIETY

pubs.acs.org/JPCC

Article

Rerouting Pathways of Solid-State Ammonia Borane Energy Release

Prithwish Biswas,[§] Pankaj Ghildiyal,[§] Hyuna Kwon, Haiyang Wang, Zaira Alibay, Feiyu Xu, Yujie Wang, Bryan M. Wong, and Michael R. Zachariah*

Cite This: *J. Phys. Chem. C* 2022, 126, 48−57

Read Online

ACCESS | Metrics & More | Article Recommendations | Supporting Information

ABSTRACT: Ammonia borane (NH_3BH_3, AB) represents a promising energy-dense material for hydrogen storage and propulsion; however, its energy release mechanisms on oxidation by solid-state oxidizers are not well understood. In this study, through in situ time-of-flight mass spectrometry supported by attenuated total reflection-Fourier transform infrared spectroscopy and density functional theory calculations, we investigate the fundamental reaction mechanisms involved in the energy release from solid-state AB with different chemical oxidizers. We show that the reaction of AB with oxidizers like $KClO_4$ is mediated by $[NH_3BH_2NH_3]^+[BH_4]^-$ (DADB) formation, resulting in its kinetic entrapment into low-energy BNH_x clusters that are resistant to further oxidation, thus limiting complete energy extraction. In contrast, with an ammonium-based oxidizer such as NH_4ClO_4, the presence of NH_4^+ ions enables AB to follow an alternative reaction pathway forming $[NH_3BH_2NH_3]^+[ClO_4]^-$ rather than DADB, thus inhibiting the formation of BNH_x species and facilitating its complete oxidation. This alternative reaction route causes the AB/NH_4ClO_4 system to exhibit remarkably higher energy release rates over that of AB/$KClO_4$ (~27x) and the standard Al/NH_4ClO_4 propellant (~7x).

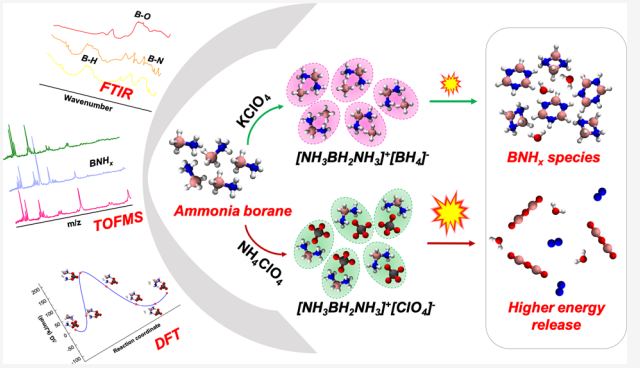

1. INTRODUCTION

Ammonia borane (AB) and other chemical hydrides[1−7] possess higher enthalpy of oxidation than commonly employed metallic or metalloid fuels in solid-state propellants such as Al, Ti, Si, and Mg,[8−12] on both a gravimetric and molar basis (Figure 1). Owing to its high gravimetric hydrogen content (19.6%) and low hydrogen generation temperature, AB has found considerable interest in the hydrogen storage application communities as has investigation of its dehydrogenation mechanism.[13−22] However, for its application in solid-state propellants, complete oxidation of the constituent boron in addition to hydrogen is essential to exploit its high energy content.

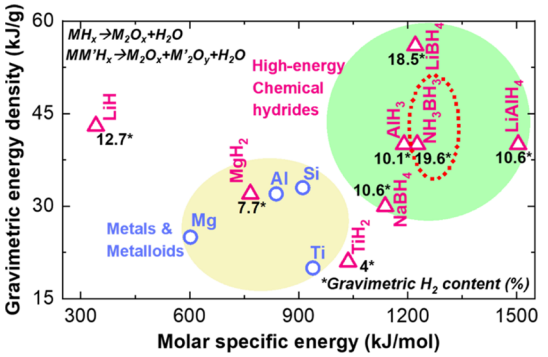

Figure 1. Gravimetric energy density, hydrogen content, and molar specific energy of chemical hydrides (balanced reactions in Figure S1), showing AB (NH_3BH_3) has a theoretically higher energy content than most metals and metalloids.

Previous studies on AB hypergolic ignition and combustion have only explored its role as an additive in enhancing the combustion kinetics of liquid propellants.[23−27] In liquid propellants, which usually consist of strong oxidizing acids, AB hydrolysis facilitates the formation of borates leading to its complete oxidation and high energy release.[25] However, thermolysis of solid-state AB can result in its oligomerization between ~370 and 450 K, generating relatively stable boron−nitrogen−hydrogen (BNH_x) compounds such as borazine, polyaminoboranes (p-ABs), polyiminoboranes (p-IBs), polyborazylene (p-BZ), and even boron nitride (BN).[28−35] Most of these BNH_x species, being structurally analogous to aromatic hydrocarbons,[36] likely have poor combustion kinetics and energy release rates[37−39] than elemental B and H, which may

Received: October 14, 2021
Revised: December 14, 2021
Published: December 29, 2021

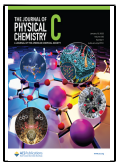

https://doi.org/10.1021/acs.jpcc.1c08985
J. Phys. Chem. C 2022, 126, 48−57

negatively affect the energetic performance of AB-based propellants.

In solid propellants, physical and chemical processes occurring in the flame preheating zones,[40−42] which exist below the ignition temperature, play a significant role in controlling their propagation and energy release rate. The generation of oxidation-resistant BNH_x species (∼373−450 K) in the preheating zone might also affect the energy release profiles of AB-based propellants. Studies on AB thermolysis at heating rates of 1−20 K/min have shown that the release of BNH_x varies with increasing heating rates.[43−46] Because the preignition zone in propellant systems is subjected to much higher heating rates of $\sim 10^5$ K/s,[47] it is essential to first identify the BNH_x species released from AB at high heating rates, something which has not been studied before. Furthermore, to assess the applicability of AB as a fuel in propellant systems, it is also essential to study the role of the BNH_x species in the energy release profile of AB with different solid-state oxidizers.

In this study, we provide a mechanistic clarification of the release of BNH_x species and their role in the combustion reaction of AB with different solid-state chemical oxidizers. Using in situ time- and temperature-resolved measurements supported with density functional theory (DFT) computations, we show that the energetic components (boron and hydrogen) of AB get kinetically trapped into BNH_x species prior to the oxygen evolution from most oxidizers even at high heating rates ($\sim 10^5$ K/s), resulting in its slower kinetics and lower energy release. Interestingly, we observe that with ammonium perchlorate/NH_4ClO_4 (AP) as an oxidizer, AB follows a distinctly different energy release pathway, where AB and AP molecules synergistically form a new intermediate that inhibits the formation of BNH_x species, leading to more complete oxidation of AB. This alternative reaction pathway also leads to faster kinetics (∼27x) and energy release of AB with AP compared to AB with $KClO_4$ as an oxidizer. This effective rerouting of the thermochemical oxidation pathway of AB with AP also results in its ∼7x faster energy release rates than the standard propellant aluminum (Al/AP) system, thus demonstrating AB as a reactive, primary fuel in solid-state propellant systems.

2. METHODS

2.1. Materials and Characterization. AB (∼97%) and hexadecyltrimethylammonium bromide/CTAB (∼98%) were obtained from Sigma-Aldrich, and AP and potassium perchlorate ($KClO_4$) were procured from Fluka. Solvents (hexane and ethanol) and salts (sodium hydroxide and ammonium chloride) were obtained from Fischer-Scientific. The oxidizer particles ($KClO_4$ and AP) were size-reduced by spray drying, following similar procedures described elsewhere.[48,49] CuO (∼50 nm) particles were obtained from US Research Nanomaterials, and ∼90−210 nm Bi_2O_3 was obtained from Sigma-Aldrich. 50 nm Aluminum nanoparticles (ALEX) were procured from Argonide Corp., which have similar characteristics as described in previous publications.[50]

XRD spectra of different samples were obtained through a PANalytical EMPYREAN equipped with a Cu Kα source (λ = 1.543 Å). A Nova NanoSEM 450 has been used to obtain SEM micrographs of different samples. Thermogravimetric-differential scanning calorimetry of different samples was performed using a Netzsch TGA/DSC apparatus typically under Ar flow at 10 K/min, unless otherwise mentioned.

A fuel/oxidizer system has been prepared by physically mixing the synthesized solid AB particles (Section 2.2) dispersed in hexane, with respective solid oxidizer particles through sonication, in stoichiometric ratios (Section S5.1) considering complete oxidation of the fuel. The sonicated dispersion is directly used for sample preparation in T-jump TOFMS (Section 2.3) measurements or else vacuum dried at room temperature and used for attenuated total reflection-Fourier transform infrared (ATR-FTIR) (Section 2.4), TGA/DSC, and combustion cell measurements (Section 2.5).

2.2. Synthesis of Size-Reduced AB. The as-received AB particles were dissolved in ethanol (treated with 10^{-5} M NaOH) to make a solution of strength 0.87 M, which is half of the solubility limit of AB in ethanol.[30] CTAB powder is then added to the AB solution in ethanol, such that the final concentration of CTAB in the solution is 0.12 M, which is about half of its critical micellar concentration in ethanol.[51] After the solutes are fully dissolved, the AB/CTAB solution in ethanol is added dropwise to hexane (antisolvent) under vigorous stirring, in a manner such that the ratio of the volume of the solvent to antisolvent in the final mixture is 1:3. The entire process was carried out in a temperature-controlled environment at 40 °C. The dispersion of particles formed in the solvent−antisolvent mixture is then separated by centrifuging. The separated particles are washed with antisolvent two times, centrifuged, and then left for overnight vacuum drying at room temperature. The AB and CTAB concentration are optimized to obtain the desired particle size and mass fraction of CTAB coating.

2.3. T-Jump TOFMS and Ignition Temperature Measurements. A T-jump time of flight mass spectrometer is used for the time- and temperature-resolved in situ identification of the gas-phase species formed during rapid reactions, a detailed description of which can be found elsewhere.[52,53] The sample is loaded by coating on a Pt wire (length ∼ 0.8 cm, diameter ∼ 76 μm, Omega Engineering, Inc.) and pulse-heated to ∼1500 K within 3 ms at a heating rate of $\sim 10^5$ K/s. The gaseous species generated on heated activation of the sample are ionized by 70 eV electrons. The positive ions are electrically accelerated through the time-of-flight tube to the multichannel plate detector, and the spectra are obtained for 10 ms at 0.1 ms intervals. The temperature of the wire is monitored by probing the current and voltage across the wire, at 0.1 ms intervals for the entire width of the heating pulse. The ignition measurements, with a detailed description in refs 10 and 54, consist of the same Pt wire, and the sample is loaded and heated in the same manner, with the same temperature probe. Additionally, in this case, the Pt wire is loaded on a different sample holder, which is provisioned to be inserted into a specialized chamber equipped with an inlet and outlet for flowing of gases, an outlet for applying vacuum, a pressure gauge, and a wall made of quartz glass for high-speed imaging of the sample on the wire. All ignition measurements were conducted under 1 atm of Ar. The ignition delay time is estimated from the video captured with ∼μs resolution by a high-speed camera (Vision Research Phantom V12.1) and correlated with the measured wire temperature to determine the ignition temperature.

2.4. ATR-FTIR Measurements. ATR-FTIR characterization of solid powders was performed on a Nicolet iS50R spectrometer with a deuterated triglycine sulfate detector. All the spectra were collected at 4 cm^{-1} resolution. The spectra obtained were averaged every 60 s (40 scans/spectrum) and

https://doi.org/10.1021/acs.jpcc.1c08985
J. Phys. Chem. C 2022, 126, 48−57

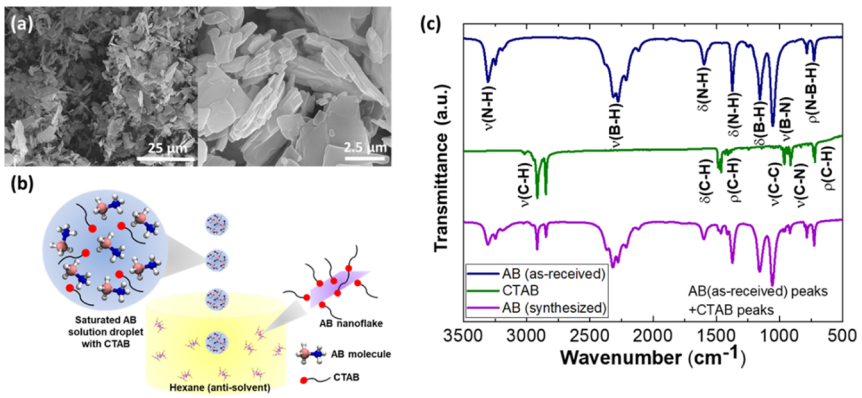

Figure 2. (a) SEM images of synthesized AB nanoflakes with a thickness of 75−325 nm. (b) Synthesis of AB nanoflakes by antisolvent crystallization in the presence of CTAB. (c) ATR-FTIR confirming the synthesized material contains both CTAB and AB.

Scheme 1. One of the Widely Accepted Pathways of AB Decomposition

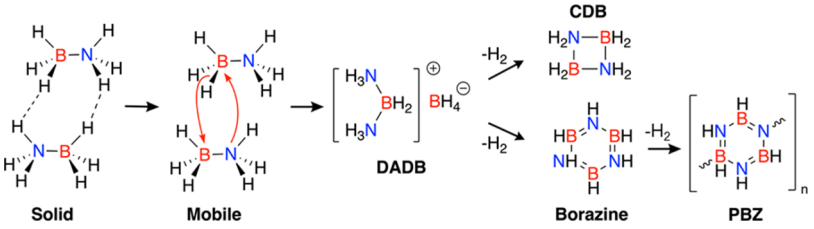

processed using Happ-Genzel apodization, Mertz phase correction, and atmospheric suppression using dry KBr as ref 55.

2.5. Temporal Characterization of Self-Propagating Reaction by a Constant-Volume Combustion Cell. Constant-volume combustion cell (~20 cm^3) measurements were performed on dry powder mixtures of fuel and the oxidizer for temporal characterization of the self-propagating combustion reaction. Fuel/oxidizer systems have been prepared in the same manner as described in Section 2.1 During each combustion cell measurement, 25 mg of the premixed fuel/oxidizer powder was tested under ambient atmospheric pressure. In a typical combustion cell measurement, the powdered sample is placed under a nichrome wire such that the wire only touches the center of the top surface of the powdered sample. The nichrome wire is resistively heated to ignite the sample, and the sample is allowed to self-propagate after ignition. The time-dependent pressure signal was obtained using a high-frequency pressure transducer (PCB Piezoeltronics). A photomultiplier tube (Hamamatsu) connected to the combustion cell through an assembly of a convex lens and fiber optic cable has been used to measure the optical emission to characterize burn time. More information on this measurement can be found in an earlier publication.[10]

2.6. DFT Calculations. All the molecules were optimized in periodic 15 × 15 × 15 Å-sized unit cells using the ab initio DFT method in the generalized gradient approximation of Perdew−Burke−Ernzerhof (PBE).[56] Plane-wave basis and projector augmented wave (PAW) pseudopotentials provided by the Vienna Ab initio Simulation Package (VASP) have been used. We only investigated the Γ-point of the Brillouin zone in all the unit cells. We employed the following cutoff values: the energy cutoff was 300 eV, force cutoff was 10^{-2} eV/Å, and energy convergence cutoff was 10^{-6} eV.

After optimizing the structures of each molecule, we used the climbing image nudged elastic band (CI-NEB) method to find the transition state.[57,58] We used five or seven images to calculate the reaction path. The images in the simulation were relaxed until the forces reduced to the cutoff force, which is 10^{-2} eV/Å. Optimized structures and fractional coordinates are included in Sections S5.2 and S5.3.

3. RESULTS AND DISCUSSION

3.1. Synthesis and Characterization of Nanoflakes of AB. AB is synthesized by an antisolvent crystallization method as described in Section 2.2. Because the size of the as-received material is not immediately suitable for our application, we conducted a recrystallization to reduce the particle size. Dropwise addition of an alkaline ethanol-based saturated solution of AB with dissolved CTAB to the antisolvent (hexane) under vigorous stirring (Figure 2b) leads to the nucleation and growth of AB nanoflakes shown by the SEM images in Figure 2a. The steric interactions of the cationic surfactant CTAB coupled with the enhanced diffusivity of the recrystallizing AB nuclei due to vigorous stirring of the antisolvent restrict the thickness of the nanoflakes between 75 and 325 nm (Figure S2a), with a modal thickness of ~175 nm, which is drastically lower compared to the agglomerated ~100 μm commercial AB particles (Figure S2c).

Figure 2c shows that the synthesized AB has the FTIR peaks of both AB and CTAB,[13] proving the formation of AB particles with CTAB on the surface, as also shown by the XRD spectra (Figure S2b, Supporting Information). In TGA/DSC measurement, the synthesized AB shows a similar mass loss (Figure S3b) to the as-received AB (Figure S3a), indicating that the active content of AB molecules is preserved after recrystallization of the nanoflakes.

3.2. Thermolytic Entrapment of AB into BNH_x Species. Prior studies on AB thermolysis under an anaerobic environment have reported that AB molecules tend to oligomerize at high temperatures to form BNH_x species such

https://doi.org/10.1021/acs.jpcc.1c08985
J. Phys. Chem. C 2022, 126, 48−57

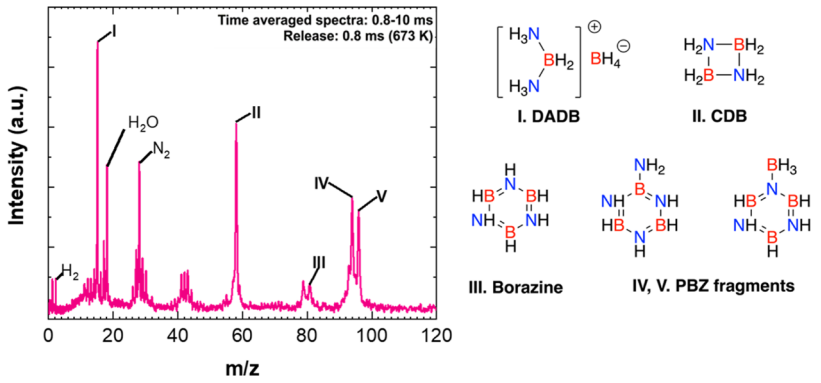

Figure 3. Time-averaged T-jump TOFMS spectra (0.8−10 ms) showing DADB and different BNH_x species borazine, CDB, and PBZ are released from AB thermolysis at a high heating rate of ~10^5 K/s.

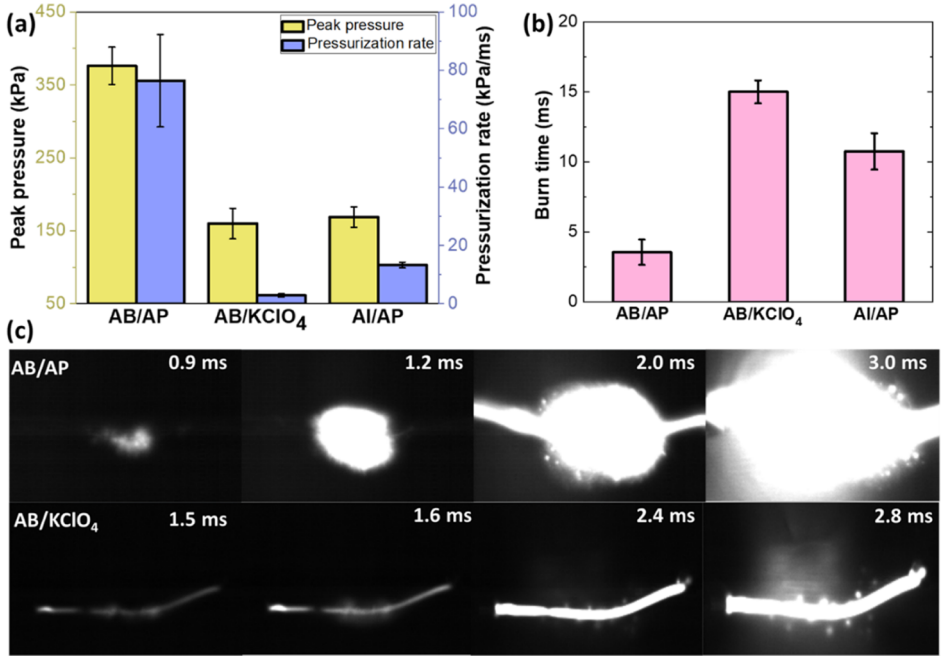

Figure 4. Combustion cell experiments showing that the peak pressure (a) and pressure rise rates (b) of AB/AP is significantly higher than those of Al/AP and AB/$KClO_4$. (c) Time-resolved snapshot of the ignition process showing that the AB/AP flame is more violent and brighter than AB/$KClO_4$.

as borazine, p-ABs, p-IBs, and p-BZ. Scheme 1 shows one of the widely accepted pathways[28,32] of AB decomposition through diammoniate of diborane (DADB) formation:

Strong dihydrogen bonding exists between the heteropolar hydrogens of AB molecules ($NH^{\delta+}\cdots^{\delta-}HB$) in the solid state. Heating disrupts the dihydrogen bonds and melting of AB to a mobile phase, in which the interaction between the N and B atoms of different AB molecules leads to the formation of DADB. DADB then rearranges to form gaseous cyclic diborane (CDB) after releasing H_2 or alternatively reacts with excess AB to form gas-phase borazine and H_2. Borazine can further dehydrogenate and polymerize to form polyborazylene (PBZ) as the final solid-state decomposition product.

Previous TGA/DSC, FTIR, and mass spectrometric studies on thermal decomposition of AB at different heating rates (1−50 K/min; <1 K/s) have reported that the amount of gas-phase products increases with an increase in heating rate.[43,46] As high heating rates (~10^5 K/s) are required for the ignition of energetic materials, we performed temperature jump time-of-flight mass spectrometry (T-jump/TOFMS) at ~10^5 K/s for in situ time- and temperature-resolved probing of gas-phase species released from AB decomposition under actual ignition conditions (Section 2.3). The sample is shock-heated to 1500 K within 3 ms (~10^5 K/s), and the mass spectra, acquired over 10 ms at an interval of 0.1 ms, show the release of different BNH_x species at ~0.8 ms (623 ± 6 K) (Figure S4). Time-averaged mass spectra from the release time (~0.8 ms) to 10 ms (Figure 3) reveal the release of H_2 (m/z = 2) and boron−nitrogen−hydrogen (BNH_x) species such as CDB (m/z = 58), borazine (m/z = 81), and PBZ fragments (m/z = 94 and 96) during thermolysis of AB at 10^5 K/s. The appearance of the strong BH_4 (m/z = 15) peak likely indicates the formation of DADB ($[NH_3BH_2NH_3]^+[BH_4]^-$). T-jump TOFMS on standard borohydride salts like $NaBH_4$ shows peaks of both the cation (Na) and anion (BH_4) (Figure S16b), which appear because of either thermal or electron impact ion dissociation of the salt. Therefore, the m/z = 15 peak likely appears due to BH_4 released from DADB, whereas its cation might have fragmented into smaller species resulting in the small peaks observed at m/z = 13−17. Hence, the observation of DADB,

https://doi.org/10.1021/acs.jpcc.1c08985
J. Phys. Chem. C 2022, 126, 48−57

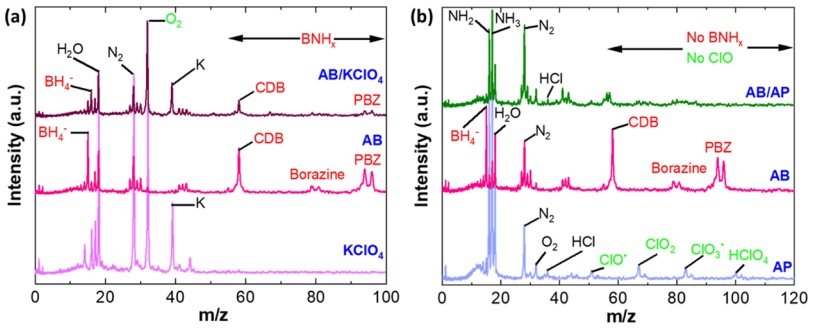

Figure 5. (a) T-jump TOFMS showing the evolution of BNH_x, K, and O_2 in AB/$KClO_4$ reaction. (b) Both BNH_x and ClO_x species are absent in the T-jump TOFMS spectra of AB/AP reaction, indicating AB/AP redox reaction follows a distinct condensed phase pathway.

CDB, borazine, and PBZ suggests that thermal decomposition of AB at ~10^5 K/s under anaerobic conditions follows Scheme 1.

Thus, even at higher heating rates, the elemental energetic constituents (B and H) of AB get trapped into BNH_x species, which are analogous to aromatic hydrocarbons. Hence, these species will have poor oxidation and combustion kinetics with low energy release rates. The implications of the release of these species on energy release rates from AB oxidation and combustion, along with a method of chemically overcoming the formation of these species, have been studied and discussed in the subsequent sections.

3.3. Ignition and Self-Propagation Reaction Rates of AB with Different Oxidizers. Metal oxides like CuO (O_2 release ~940 K) and Bi_2O_3 (O_2 release ~1220 K) and oxysalts like $KClO_4$ (O_2 release ~870 K) and NH_4ClO_4 (O_2 release ~670 K) are commonly employed as oxidizers in solid-state energetic formulations.[59,60] The O_2 release temperatures of these oxidizers were also measured by T-jump TOFMS at a heating rate of ~10^5 K/s (Figure S5). To probe the energy release profile of AB, ignition temperature (Section 2.3) and constant-volume pressurization (Section 2.5) rate measurements have been performed on ultrasonically mixed powders of AB nanoflakes with respective oxidizer particles in stoichiometric proportions (Section 2.1). The ignition temperature measurements were performed under 1 atm of Ar, so that the solid-state oxidizers act as the only oxygen sources.

Figure 4a compares the pressure and pressurization rates between AB/AP, AB/$KClO_4$, and the standard propellant, Al/AP (control system), obtained from constant-volume combustion cell measurements. The pressurization rate is estimated from the slope of a linear fit from the pressure rise point to the peak pressure in the acquired pressure signal (Figure S6). AB/AP reaction (peak pressure of ~380 kPa) outperforms the AB/$KClO_4$ reaction (peak pressure ~120 kPa), as well as the standard propellant Al/AP reaction (peak pressure of ~150 kPa). The pressurization rate of AB/AP reaction (76.5 kPa/ms) is ~27 times higher than that of AB/$KClO_4$ and about ~7 times higher than that of the standard propellant Al/AP. Figure 4b shows the burn times characterized by the FWHM of the normalized optical signals (Figure S6) obtained during the same measurement. AB/AP has a burn time of ~3 ms, which is ~1/5 of AB/$KClO_4$ and ~1/3 of Al/AP. The significantly higher pressurization rates and shorter burn times indicate the superior reactivity and energy release rate of the AB/AP system. No ignition or combustion is observed for AB/CuO and AB/Bi_2O_3 systems, indicating the poor reactivity of AB with CuO and Bi_2O_3.

In the time-resolved snapshots from the video obtained during ignition measurement of AB/AP and AB/$KClO_4$ (Figure 4c), the AB/AP flame looks brighter and more violent than AB/$KClO_4$, also qualitatively indicating higher flame-temperature and hence energy release from AB/AP. The measured ignition temperatures of both AB/AP (703 ± 11 K) and AB/$KClO_4$ (850 ± 14 K) systems are approximately the same as the O_2 release temperature of the respective oxidizers. As AB already thermolyzes into inert BNH_x species, at much lower temperatures of ~623 K (Section 3.2), the lower O_2 release temperature of AP cannot solely explain the much higher reactivity of the AB/AP system compared to AB/$KClO_4$. This indicates AB/AP reaction follows an alternative route, rather than simply getting oxidized by O_2 released from oxidizer decomposition, the mechanism of which has been investigated and discussed in the subsequent sections.

3.4. Absence of BNH_x Species in AB/AP Reaction. Gas-phase species released during the reaction of AB with $KClO_4$ and AP were temporally probed by T-jump TOFMS at the same heating rate of ~10^5 K/s. In Figure 5a, T-jump TOFMS spectra of AB/$KClO_4$ reaction show the release of the same BNH_x species as observed in the case of pristine AB, along with additional peaks for K (m/z = 39) and O_2 (m/z = 32) from $KClO_4$ decomposition. Hence, during AB/$KClO_4$ reaction, AB thermolyzes into BNH_x species through DADB formation following Scheme 1 (Section 3.2). Because pristine AP thermally decomposes through the formation of NH_3 and $HClO_4$, gaseous ClO_x species, such as $HClO_4$ (m/z = 100), ClO_2 (m/z = 67), ClO_3 (m/z = 93), and ClO (m/z = 51), are observed in the T-jump TOFMS spectra of pristine AP (Figure 5b). Interestingly, during AB/AP reaction (Figure 5b), both BNH_x species from AB thermolysis and ClO_x species from AP decomposition are absent. The peak of HCl (m/z = 36), which can only be released on complete reduction of the perchlorate anion of AP, indicates a redox reaction has occurred between AB and AP.

Upon complete oxidation, AB should form solid oxides of boron (B_2O_3 or other borates), N_2 (or nitrogen oxides), and H_2O. The BNH_x species observed in the case of AB/$KClO_4$ reaction implies that most of the elements (B, N, and H) of AB got trapped into these species. A small amount of unpolymerized AB or lighter BNH_x species (CDB or borazine) may be oxidized by O_2 released from $KClO_4$, which led to its ignition and combustion with poor kinetics. The absence of any gas-phase species containing B atoms in AB/AP indicates that B is completely oxidized to boron oxides in the condensed phase. Moreover, the absence of any ClO_x species from AP implies that AP is interacting with molten AB to form a

https://doi.org/10.1021/acs.jpcc.1c08985
J. Phys. Chem. C 2022, 126, 48−57

Scheme 2. Distinct Intermediary Pathways Followed by AB/$KClO_4$ and AB/AP Reactions

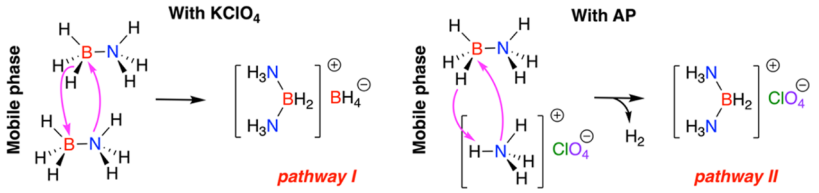

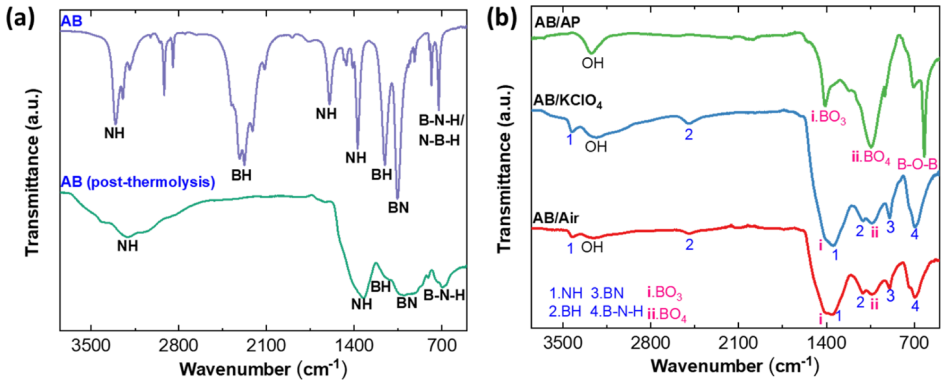

Figure 6. ATR-FTIR spectra of the (a) post-thermolysis product of AB in Ar (anaerobic) shows NH, BH, and BN bonds indicating PBZ formation, (b) oxidation products of AB/air and AB/$KClO_4$ consisting of a mixture of PBZ (NH, BH, and BN peaks) and boron oxides (BO_3 and BO_4 peaks), whereas the AB/AP product only contains boron oxides indicating complete AB oxidation with AP.

different intermediate instead of DADB, which inhibits the formation of BNH_x species and leads to the oxidation of AB in a condensed phase.

To further investigate this phenomenon, we performed T-jump TOFMS of the AB/AP mixture with excess AB (2:1 by moles). The BNH_x species like CDB and borazine are observed in the spectra of the AB/AP mixture with excess AB (Figure S7), indicating that only the amount of AB molecules present in stoichiometric equivalence to AP participates in the condensed phase redox reaction and the excess AB forms BNH_x species though DADB. This mixture also did not ignite, implying poor kinetics and inferior energy release due to BNH_x formation. Previous ^{11}B NMR studies have reported that in the presence of NH_4Cl, AB forms $[NH_3BH_2NH_3]^+[Cl]^-$ upon melting, instead of DADB ($[NH_3BH_2NH_3]^+[BH_4]^-$), because of the interaction between the N of the NH_4^+ ion of NH_4Cl and B of the AB molecule.[29] By performing T-jump TOFMS of AB/NH_4Cl mixtures with different molar ratios, we also found that BNH_x species only appear when excess AB is present (Figure S8). Based on these observations, it can be hypothesized that with NH_4ClO_4, AB forms $[NH_3BH_2NH_3]^+[ClO_4]^-$ as described in Scheme 2:

AP is well known to decompose to NH_3 and $HClO_4$.[49] Because AB decomposes to BNH_x (Figure S4) species at a lower temperature compared to AP (Figure S5), the possibility of alternative pathways through acid-catalyzed hypergolic ignition[25] of AB with $HClO_4$, released on AP decomposition, can be eliminated. The emergence of $[NH_3BH_2NH_3]^+[ClO_4]^-$ in place of DADB not only implies that the formation of BNH_x species is inhibited but also indicates that the fuel ($[NH_3BH_2NH_3]^+$) and oxidizer ($[ClO_4]^-$) component are placed into the same molecule. Usually, the reaction kinetics of particulate energetic materials is limited by the diffusion of oxygen from oxidizer particles to fuel particles, which in turn depends on the particle size. However, in intermediates like $[NH_3BH_2NH_3]^+[ClO_4]^-$, molecular level mixing of the fuel and oxidizer will drastically decrease the diffusion time scales, which might also explain the condensed phase initiation (Figure 5b) and fast kinetics of AB/AP redox reaction (Section 3.3). More analysis and discussion on this phenomenon are included in subsequent sections.

3.5. Solid-State Products of AB Oxidation. TGA/DSC measurements of AB in Ar at 10 K/min (Figure S3b) show a two-step mass loss out of which the first mass loss step feasibly corresponds to CDB formation, whereas the second mass loss step corresponds to the release of borazine as explained in Section S2.1 (Supporting Information). ATR-FTIR of the residual post-thermolysis product (~44% by wt) shows that it contains bending, stretching, and rocking vibration bands from NH, BH, BN, and BNH groups, indicating the formation of PBZ (Figure 6a). The relatively low intensity of BH bands shows that the PBZ formed is deficient in BH bonds compared to NH bonds. These observations are consistent with the BNH_x species, including PBZ fragments, observed by T-jump TOFMS (Figure 3) at high heating rates (~10^5 K/s). However, precisely, the relative amounts of gas-phase product species may be higher at high heating rates.[43]

TGA/DSC of AB in air at 10 K/min shows a ~28% mass loss in a single-step around the melting point (~383 K) of AB (Figure S9). Ideally, if AB is completely oxidized (Table 1), then 1 mol of AB should form 0.5 mol of B_2O_3 resulting in ~12% mass gain. Hence, heating in air cannot completely oxidize AB, and the ~28% mass loss may be due to gaseous BNH_x species release. TGA/DSC of AB/$KClO_4$ in Ar (Figure S10) at the same heating rate shows similar mass loss (~16%) between 390 and 450 K to that observed in TGA of pristine AB in Ar (Figure S3b), followed by a mass loss around 873 K due to $KClO_4$ decomposition. However, TGA/DSC of AB/AP under the same conditions completely differs from both pristine AB and AP (Figure S11), as no significant mass loss is observed till 436 K which also indicates that AB/AP reaction proceeds through a distinct intermediate formation in the

https://doi.org/10.1021/acs.jpcc.1c08985
J. Phys. Chem. C 2022, 126, 48−57

Table 1. Reaction Enthalpy of the (1) DADB Pathway (Borazine Formation) and (2) AB/AP Pathway (Complete Oxidation) and the Total Thermodynamic Enthalpy of (3) AB/$KClO_4$ and (4) AB/AP Reaction

Reactions	Enthalpy[a] (kJ/mol of AB)
Reaction Enthalpies Considering Different Kinetics	
(1) $3AB(NH_3BH_3) + 3O_2 \rightarrow$ borazine$(B_3N_3H_6) + 6H_2O$	−522
(2) $4AB + 9O_2 \rightarrow 2N_2 + 2B_2O_3 + 12H_2O$	−1226
Total Thermodynamic Reaction Enthalpies	
(3) $8AB + 9KClO_4 \rightarrow 4B_2O_3 + 4N_2 + 24H_2O + 9KCl$	−1233
(4) $10AB + 18AP \rightarrow 5B_2O_3 + 14N_2 + 57H_2O + 18HCl$	−1510

[a]NIST Standard ΔH_f used for all species, except for AB ΔH_f = −133.4 kJ/mol.[65]

condensed phase. ATR-FTIR is performed on the residual solid-state oxidation products of AB in air, AB/$KClO_4$, and AB/AP obtained from TGA/DSC measurement (Figure 6b). Both the oxidation products of AB in air and AB/$KClO_4$ show the presence of NH, BH, BN, and BNH groups (Figure 6b), like pristine AB decomposition in Ar (Figure 5a), indicating the formation of PBZ. Small peaks of BO_3 and BO_4 units are also observed in both cases of AB/air and AB/$KClO_4$ (Figure 6b), indicating the possible oxidation of some surface AB molecules or low molecular weight BNH_x species. However, the product of AB/AP (Figure 6b) shows strong peaks from BO_3 and BO_4 units along with rocking vibration from B−O−B units, indicating the presence of boron oxides.[61,62] Moreover, NH, BH, BN, and BNH groups are also absent in the AB/AP product, indicating the absence of PBZ.

Hence, it can be inferred from these observations that AB/AP reaction leads to complete oxidation of B atoms of AB to boron oxides, which is consistent with the observations in Section 3.4. The presence of both BO_3 and BO_4 units suggests that the product contains mixed boron oxides,[63,64] where BO_3 and B−O−B bands suggest the formation of boric anhydride/B_2O_3 (Figure S12), BO_4 units indicate the formation of cyclic borates, and OH groups suggest the formation of some boric acid ($B(OH)_3$). The complete oxidation of AB with AP also explains the superior energy release and combustion kinetics of AB/AP redox reaction compared to AB/$KClO_4$ as observed in Section 3.3.

3.6. Energetics of AB/AP Reaction from DFT and Discussion. In Section 3.2, we observed that AB thermolysis occurs through DADB ($[NH_3BH_2NH_3]^+[BH_4]^-$) formation which results in its oligomerization into BNH_x species like CDB, borazine, and PBZ. With $KClO_4$ and air, AB also undergoes thermolysis to form DADB, CDB, borazine (Section 3.4), and PBZ (Sections 3.4 and 3.5), additionally forming some boron oxides (Section 3.5). With AP, AB possibly forms $[NH_3BH_2NH_3]^+[ClO_4]^-$ (Section 3.4) as an intermediate instead of DADB, which results in its complete oxidation to boron oxides (Section 3.5). Hence, BNH_x species are absent in AB/AP reaction (Sections 3.4 and 3.5).

To further evaluate the possibility of $[NH_3BH_2NH_3]^+[ClO_4]^-$ formation during AB/AP reaction in place of DADB, the energetics of the formation of DADB and $[NH_3BH_2NH_3]^+[ClO_4]^-$ are evaluated through DFT calculation (Section 2.6). Figure 7 shows a comparison between the free-energy diagrams of $[NH_3BH_2NH_3]^+[ClO_4]^-$ formation (Figure 7a) and DADB formation (Figure 7b). On AB/AP reaction, a negative free energy change ($\Delta G \sim -57.2$

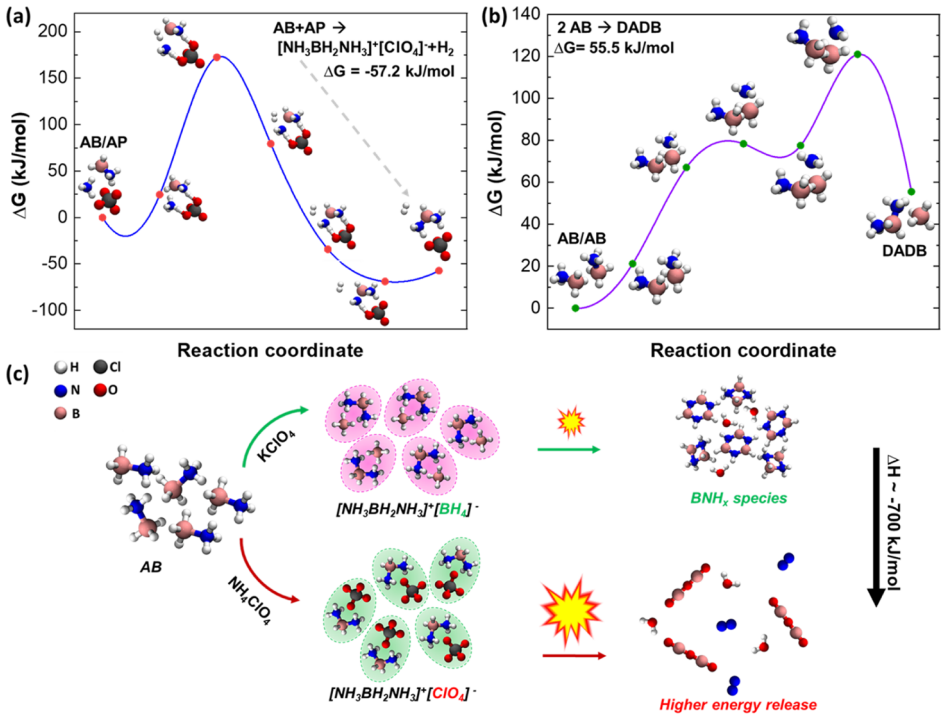

Figure 7. Free energy diagram of the $[NH_3BH_2NH_3]^+[ClO_4]^-$ formation ($\Delta G \sim -57.2$ kJ/mol) through the AB/AP pathway (a) and DADB formation ($\Delta G \sim 55.5$ kJ/mol) through AB oligomerization (b), demonstrating a higher feasibility of $[NH_3BH_2NH_3]^+[ClO_4]^-$ formation through AB/AP reaction. (c) Schematic of the studied thermochemical oxidation mechanisms of AB, illustrating the alternative AB/AP reaction route leads to complete oxidation of AB and ~700 kJ/mol higher energy release than AB/$KClO_4$.

https://doi.org/10.1021/acs.jpcc.1c08985
J. Phys. Chem. C 2022, 126, 48−57

kJ/mol) indicates the higher feasibility of $[NH_3BH_2NH_3]^+[ClO_4]^-$ formation over DADB ($\Delta G \sim 55.5$ kJ/mol). Furthermore, as the fuel ($[NH_3BH_2NH_3]^+$) and oxidizer ($[ClO_4]^-$) are mixed at the molecular level in $[NH_3BH_2NH_3]^+[ClO_4]^-$, the rate of its redox decomposition will not be limited by oxygen diffusion. Hence, the intramolecular redox reaction of $[NH_3BH_2NH_3]^+[ClO_4]^-$ will have extremely fast kinetics.

Thus, with only AP as an oxidizer (Figure 7c), the formation of $[NH_3BH_2NH_3]^+[ClO_4]^-$ will inhibit the formation of BNH_x species ensuring the complete oxidation of AB resulting in its superior energy release profile. With $KClO_4$ and other oxidizers, the formation of DADB, will trap the elemental constituents of AB (B, N, and H) into BNH_x species, resulting in its incomplete oxidation and inferior energy release profile. Table 1 shows borazine formation through the DADB pathway and creates at least ~700 kJ/mol deficit in energy release compared to its complete oxidation through the AB/AP pathway. This energy deficit is much higher than the ~280 kJ/mol difference in total thermodynamic reaction enthalpy between AB/AP and AB/$KClO_4$ (Table 1), establishing the significance of an alternative pathway on the energy release profile of AB. The higher exothermicity of the AB/AP pathway leads to greater heat generation during the AB/AP combustion reaction, causing a temperature increase, and an accelerated reaction rate. These factors explain the poor combustion kinetics of AB/$KClO_4$ and the non-ignitability of AB with CuO and Bi_2O_3. Additionally, the superior performance of AB/AP compared to the standard Al/AP propellant system shows that AB can be potentially used as a major fuel component in solid-state propellant systems.

At the particle level, molten AB possibly reacts with the surface molecules of NH_4ClO_4 particles forming $[NH_3BH_2NH_3]^+[ClO_4]^-$ following a shrinking-core model.[66] When the external temperature ramp causes melting of AP, the rate of formation of $[NH_3BH_2NH_3]^+[ClO_4]^-$ is enhanced. We can hypothesize that with other NH_4^+ based oxidizers, such as ammonium dinitramide ($NH_4N_3O_4$) and ammonium nitrate (NH_4NO_3), AB will also form $[NH_3BH_2NH_3]^+$[oxidizer anion] as an intermediate. Therefore, these oxidizers may also show high reactivity with solid AB. However, because these ammonium salts with different anions have different melting points, the oxidative energy release profile of AB can be further tuned by changing the anions of NH_4^+-based oxidizers, which we plan to investigate in our future studies.

4. CONCLUSIONS

The current study presents a mechanistic understanding of the distinct thermochemical energy release pathways of AB with different chemical oxidizers in the solid state. Through, in situ T-jump TOFMS measurements, we have shown that AB thermolyzes to BNH_x species such as CDB, borazine, and PBZ, through DADB formation, even at high heating rates (~10^5 K/s). With chemical oxidizers like $KClO_4$, T-jump TOFMS shows the formation of same BNH_x species. Additionally, ATR-FTIR confirms that the solid-state AB/$KClO_4$ reaction products contain a mixture of PBZ and boron oxides. However, with AP, complete oxidation of AB to boron oxides is observed in the absence of BNH_x species release, which can be attributed to the possible formation of $[NH_3BH_2NH_3]^+[ClO_4]^-$ as an intermediate, instead of DADB. DFT calculations show that $[NH_3BH_2NH_3]^+[ClO_4]^-$ formation ($\Delta G \sim -57.2$ kJ/mol) in AB/AP reaction has a higher feasibility over DADB ($\Delta G \sim 55.5$ kJ/mol). The formation of $[NH_3BH_2NH_3]^+[ClO_4]^-$ also eliminates oxygen diffusion limitation, thereby ensuring faster kinetics. The faster and complete oxidation of AB in the AB/AP pathway explains the higher energy release rate (~27×) of AB/AP compared to AB/$KClO_4$ in combustion cell measurements. Therefore, these mechanistic insights into the energy release profile of solid-state AB open possibilities for the rational design of materials for hydrogen storage and propulsion, by exploiting its different reaction pathways to achieve greater control over material properties and reactive characteristics.

■ ASSOCIATED CONTENT

Supporting Information

The Supporting Information is available free of charge at https://pubs.acs.org/doi/10.1021/acs.jpcc.1c08985.

SEM size distribution and XRD of AB; TGA/DSC analysis of commercial AB, AB/AP, AB/$KClO_4$, and AB/air products; temporal T-jump TOFMS of AB, $KClO_4$, and AP; ignition temperatures of AB/AP and AB/$KClO_4$; T-jump TOFMS of AB with NH_4Cl and excess AB with AP; ATR-FTIR of B_2O_3 and AB/AP products; input fractional coordinates and optimized structures for DFT calculations; SEM of combustion products; NMR of AB and thermolyzed AB; T-jump TOFMS of $NaBH_4$; and TGA/DSC of CTAB (PDF)

■ AUTHOR INFORMATION

Corresponding Author

Michael R. Zachariah − *University of California, Riverside, Riverside, California 92521, United States;* orcid.org/0000-0002-4115-3324; Email: mrz@engr.ucr.edu

Authors

Prithwish Biswas − *University of California, Riverside, Riverside, California 92521, United States;* orcid.org/0000-0002-9921-2905

Pankaj Ghildiyal − *University of California, Riverside, Riverside, California 92521, United States; University of Maryland, College Park, Maryland 20742, United States;* orcid.org/0000-0002-4422-3068

Hyuna Kwon − *University of California, Riverside, Riverside, California 92521, United States*

Haiyang Wang − *University of California, Riverside, Riverside, California 92521, United States;* orcid.org/0000-0001-5200-3965

Zaira Alibay − *University of California, Riverside, Riverside, California 92521, United States;* orcid.org/0000-0002-1335-9202

Feiyu Xu − *University of California, Riverside, Riverside, California 92521, United States; University of Maryland, College Park, Maryland 20742, United States*

Yujie Wang − *University of California, Riverside, Riverside, California 92521, United States*

Bryan M. Wong − *University of California, Riverside, Riverside, California 92521, United States;* orcid.org/0000-0002-3477-8043

Complete contact information is available at: https://pubs.acs.org/10.1021/acs.jpcc.1c08985

https://doi.org/10.1021/acs.jpcc.1c08985
J. Phys. Chem. C 2022, 126, 48−57

Author Contributions

[§]P.B. and P.G. have equal contribution. M.R.Z. initiated and supervised the project, wrote original draft. P.B. synthesized AB, performed T-jump TOFMS, ignition characterization, TGA/DSC, ATR-FTIR analysis, NMR, thermodynamic calculations, and wrote original draft. P.G. performed ATR-FTIR, critical data analyis, and wrote original draft. H.K. performed all DFT and themodynamic calculations, wrote original draft. H.W. performed SEM and helped in AB synthesis. Z.A. performed combustion cell measurements. F.X. performed XRD and synthesized $KClO_4$. Y.W. synthesized AP and helped in AB synthesis. B.M.W. supervised all DFT calculations. All other have also contributed by reviewing and editing the manuscript.

Notes

The authors declare no competing financial interest.

■ ACKNOWLEDGMENTS

We gratefully acknowledge support from the ONR and the DTRA-URA on Materials Science in Extreme Environments (*HDTRA1-20-2-0001*). We are also thankful to the CFAMM at the University of California, Riverside for supporting with microscopy instrumentation. We also acknowledge Dr. Lingchao Zhu and ACIF facility at the University of California, Riverside for supporting with NMR characterization.

■ REFERENCES

(1) Schlapbach, L.; Züttel, A. Hydrogen Storage Materials for Mobile Applications. *Nature* **2001**, *414*, 353−358.
(2) Schneemann, A.; White, J. L.; Kang, S.; Jeong, S.; Wan, L. F.; Cho, E. S.; Heo, T. W.; Prendergast, D.; Urban, J. J.; Wood, B. C.; et al. Nanostructured Metal Hydrides for Hydrogen Storage. *Chem. Rev.* **2018**, *118*, 10775−10839.
(3) Demirci, U. B.; Miele, P. Sodium Borohydride versus Ammonia Borane, in Hydrogen Storage and Direct Fuel Cell Applications. *Energy Environ. Sci.* **2009**, *2*, 627−637.
(4) Aguey-Zinsou, K.-F.; Ares-Fernández, J.-R. Hydrogen in Magnesium: New Perspectives toward Functional Stores. *Energy Environ. Sci.* **2010**, *3*, 526−543.
(5) Zhang, J.; Zhu, Y.; Lin, H.; Liu, Y.; Zhang, Y.; Li, S.; Ma, Z.; Li, L. Metal Hydride Nanoparticles with Ultrahigh Structural Stability and Hydrogen Storage Activity Derived from Microencapsulated Nanoconfinement. *Adv. Mater.* **2017**, *29*, 1700760.
(6) Ngene, P.; Longo, A.; Mooij, L.; Bras, W.; Dam, B. Metal-Hydrogen Systems with an Exceptionally Large and Tunable Thermodynamic Destabilization. *Nat. Commun.* **2017**, *8*, 1846.
(7) Cao, H.; Georgopanos, P.; Capurso, G.; Pistidda, C.; Weigelt, F.; Chaudhary, A.-L.; Filiz, V.; Tseng, J.-C.; Wharmby, M. T.; Dornheim, M.; et al. Air-Stable Metal Hydride-Polymer Composites of $Mg(NH_2)_2$−LiH and TPX. *Mater. Today Energy* **2018**, *10*, 98−107.
(8) Salvagnac, L.; Assie-Souleille, S.; Rossi, C. Layered Al/CuO Thin Films for Tunable Ignition and Actuations. *Nanomaterials* **2020**, *10*, 2009.
(9) Ghildiyal, P.; Ke, X.; Biswas, P.; Nava, G.; Schwan, J.; Xu, F.; Kline, D. J.; Wang, H.; Mangolini, L.; Zachariah, M. R. Silicon Nanoparticles for the Reactivity and Energetic Density Enhancement of Energetic-Biocidal Mesoparticle Composites. *ACS Appl. Mater. Interfaces* **2021**, *13*, 458−467.
(10) Xu, F.; Biswas, P.; Nava, G.; Schwan, J.; Kline, D. J.; Rehwoldt, M. C.; Mangolini, L.; Zachariah, M. R. Tuning the Reactivity and Energy Release Rate of I_2O_5 Based Ternary Thermite Systems. *Combust. Flame* **2021**, *228*, 210−217.
(11) Lomba, R.; Bernard, S.; Gillard, P.; Mounaïm-Rousselle, C.; Halter, F.; Chauveau, C.; Tahtouh, T.; Guézet, O. Comparison of Combustion Characteristics of Magnesium and Aluminum Powders. *Combust. Sci. Technol.* **2016**, *188*, 1857−1877.
(12) Alibay, Z.; Kline, D. J.; Rehwoldt, M. C.; Biswas, P.; Herrera, S.; Wang, H.; Zachariah, M. R. Mechanism of Microwave-Initiated Ignition of Sensitized Energetic Nanocomposites. *Chem. Eng. J.* **2021**, *415*, 128657.
(13) Valero-Pedraza, M.-J.; Cot, D.; Petit, E.; Aguey-Zinsou, K.-F.; Alauzun, J. G.; Demirci, U. B. Ammonia Borane Nanospheres for Hydrogen Storage. *ACS Appl. Nano Mater.* **2019**, *2*, 1129−1138.
(14) Wang, C.; Tuninetti, J.; Wang, Z.; Zhang, C.; Ciganda, R.; Salmon, L.; Moya, S.; Ruiz, J.; Astruc, D. Hydrolysis of Ammonia-Borane over Ni/ZIF-8 Nanocatalyst: High Efficiency, Mechanism, and Controlled Hydrogen Release. *J. Am. Chem. Soc.* **2017**, *139*, 11610−11615.
(15) Wahab, M. A.; Zhao, H.; Yao, X. D. Nano-Confined Ammonia Borane for Chemical Hydrogen Storage. *Front. Chem. Sci. Eng.* **2012**, *6*, 27−33.
(16) Yang, J. B.; Lamsal, J.; Cai, Q.; James, W. J.; Yelon, W. B. Structural Evolution of Ammonia Borane for Hydrogen Storage. *Appl. Phys. Lett.* **2008**, *92*, 091916.
(17) Gao, P.; Huang, Z.; Yu, H. Exploration of the Dehydrogenation Pathways of Ammonia Diborane and Diammoniate of Diborane by Molecular Dynamics Simulations Using Reactive Force Fields. *J. Phys. Chem. A* **2020**, *124*, 1698−1704.
(18) Stephens, F. H.; Baker, R. T.; Matus, M. H.; Grant, D. J.; Dixon, D. A. Acid Initiation of Ammonia-Borane Dehydrogenation for Hydrogen Storage. *Angew. Chem., Int. Ed.* **2007**, *46*, 746−749.
(19) Gutowska, A.; Li, L.; Shin, Y.; Wang, C. M.; Li, X. S.; Linehan, J. C.; Smith, R. S.; Kay, B. D.; Schmid, B.; Shaw, W.; et al. Nanoscaffold Mediates Hydrogen Release and the Reactivity of Ammonia Borane. *Angew. Chem., Int. Ed.* **2005**, *44*, 3578−3582.
(20) Lai, Q.; Rawal, A.; Quadir, M. Z.; Cazorla, C.; Demirci, U. B.; Aguey-Zinsou, K. F. Nanosizing Ammonia Borane with Nickel: A Path toward the Direct Hydrogen Release and Uptake of B−N−H Systems. *Adv. Sustainable Syst.* **2018**, *2*, 1700122.
(21) Simagina, V. I.; Vernikovskaya, N. V.; Komova, O. V.; Kayl, N. L.; Netskina, O. V.; Odegova, G. V. Experimental and Modeling Study of Ammonia Borane-Based Hydrogen Storage Systems. *Chem. Eng. J.* **2017**, *329*, 156−164.
(22) Rizzi, V.; Polino, D.; Sicilia, E.; Russo, N.; Parrinello, M. The Onset of Dehydrogenation in Solid Ammonia Borane: An Ab Initio Metadynamics Study. *Angew. Chem., Int. Ed.* **2019**, *58*, 3976−3980.
(23) Clements, K. A.; Baier, M. J.; Veeraraghavan Ramachandran, P.; Son, S. F. Experimental Study of Factors Affecting Hypergolic Ignition of Ammonia Borane. *J. Propul. Power* **2020**, *37*, 1.
(24) Baier, M.; Ramachandran, P. V.; Son, S. F. Characterization of the Hypergolic Ignition Delay of Ammonia Borane. *J. Propul. Power* **2018**, *35*, 1.
(25) Baier, M. J.; McDonald, A. J.; Clements, K. A.; Goldenstein, C. S.; Son, S. F. High-Speed Multi-Spectral Imaging of the Hypergolic Ignition of Ammonia Borane. *Proc. Combust. Inst.* **2021**, *38*, 4433−4440.
(26) Pfeil, M. A.; Son Prof, S. F.; Anderson Prof, W. E. Influence of Ammonia Borane on the Stability of a Liquid Rocket Combustor. *J. Propul. Power* **2014**, *30*, 290.
(27) Pfeil, M. A.; Groven, L. J.; Lucht, R. P.; Son, S. F. Effects of Ammonia Borane on the Combustion of an Ethanol Droplet at Atmospheric Pressure. *Combust. Flame* **2013**, *160*, 2194−2203.
(28) Stowe, A. C.; Shaw, W. J.; Linehan, J. C.; Schmid, B.; Autrey, T. In Situ Solid State 11B MAS-NMR Studies of the Thermal Decomposition of Ammonia Borane: Mechanistic Studies of the Hydrogen Release Pathways from a Solid State Hydrogen Storage Material. *Phys. Chem. Chem. Phys.* **2007**, *9*, 1831−1836.
(29) Heldebrant, D. J.; Karkamkar, A.; Hess, N. J.; Bowden, M.; Rassat, S.; Zheng, F.; Rappe, K.; Autrey, T. The Effects of Chemical Additives on the Induction Phase in Solid-State Thermal Decomposition of Ammonia Borane. *Chem. Mater.* **2008**, *20*, 5332−5336.
(30) Stephens, F. H.; Pons, V.; Tom Baker, R. Ammonia−Borane: The Hydrogen Source Par Excellence? *J. Chem. Soc., Dalton Trans.* **2007**, 2613−2626.

https://doi.org/10.1021/acs.jpcc.1c08985
J. Phys. Chem. C 2022, 126, 48−57

(31) Petit, J.-F.; Demirci, U. B. Mechanistic Insights into Dehydrogenation of Partially Deuterated Ammonia Borane NH_3BD_3 Being Heating to 200 °C. *Inorg. Chem.* **2019**, *58*, 489−494.
(32) Demirci, U. B. Mechanistic Insights into the Thermal Decomposition of Ammonia Borane, a Material Studied for Chemical Hydrogen Storage. *Inorg. Chem. Front.* **2021**, *8*, 1900−1930.
(33) Petit, J.-F.; Demirci, U. B. Discrepancy in the Thermal Decomposition/Dehydrogenation of Ammonia Borane Screened by Thermogravimetric Analysis. *Int. J. Hydrogen Energy* **2019**, *44*, 14201−14206.
(34) Bhunya, S.; Zimmerman, P. M.; Paul, A. Unraveling the Crucial Role of Metal-Free Catalysis in Borazine and Polyborazylene Formation in Transition-Metal-Catalyzed Ammonia-Borane Dehydrogenation. *ACS Catal.* **2015**, *5*, 3478−3493.
(35) Bachmann, P.; Düll, F.; Späth, F.; Bauer, U.; Steinrück, H.-P.; Papp, C. A HR-XPS Study of the Formation of h-BN on Ni(111) from the Two Precursors, Ammonia Borane and Borazine. *J. Chem. Phys.* **2018**, *149*, 164709.
(36) Yang, P.; Li, J.; Cheng, Z.; Zuo, S. Promoting Effects of Ce and Pt Addition on the Destructive Performances of V2O5/Γ-Al2O3 for Catalytic Combustion of Benzene. *Appl. Catal., A* **2017**, *542*, 38−46.
(37) Cofer, C. G.; Economy, J. Oxidative and Hydrolytic Stability of Boron Nitride - A New Approach to Improving the Oxidation Resistance of Carbonaceous Structures. *Carbon* **1995**, *33*, 389−395.
(38) Liu, Z.; Gong, Y.; Zhou, W.; Ma, L.; Yu, J.; Idrobo, J. C.; Jung, J.; Macdonald, A. H.; Vajtai, R.; Lou, J.; et al. Ultrathin High-Temperature Oxidation-Resistant Coatings of Hexagonal Boron Nitride. *Nat. Commun.* **2013**, *4*, 2541.
(39) Li, L. H.; Cervenka, J.; Watanabe, K.; Taniguchi, T.; Chen, Y. Strong Oxidation Resistance of Atomically Thin Boron Nitride Nanosheets. *ACS Nano* **2014**, *8*, 1457−1462.
(40) Wang, H.; Kline, D. J.; Zachariah, M. R. In-Operando High-Speed Microscopy and Thermometry of Reaction Propagation and Sintering in a Nanocomposite. *Nat. Commun.* **2019**, *10*, 3032.
(41) Wang, H.; Julien, B.; Kline, D. J.; Alibay, Z.; Rehwoldt, M. C.; Rossi, C.; Zachariah, M. R. Probing the Reaction Zone of Nanolaminates at ∼μs Time and ∼μm Spatial Resolution. *J. Phys. Chem. C* **2020**, *124*, 13679−13687.
(42) Chen, B.; Zheng, H.; Riehn, M.; Bok, S.; Gangopadhyay, K.; Maschmann, M. R.; Gangopadhyay, S. In Situ Characterization of Photothermal Nanoenergetic Combustion on a Plasmonic Microchip. *ACS Appl. Mater. Interfaces* **2018**, *10*, 427−436.
(43) Weismiller, M. R.; Wang, S. Q.; Chowdhury, A.; Thynell, S. T.; Yetter, R. A. Confined Rapid Thermolysis Studies of Ammonia Borane. *Thermochim. Acta* **2013**, *551*, 110−117.
(44) Baitalow, F.; Baumann, J.; Wolf, G.; Jaenicke-Rößler, K.; Leitner, G. Thermal Decomposition of B-N-H Compounds Investigated by Using Combined Thermoanalytical Methods. *Thermochim. Acta* **2002**, *391*, 159−168.
(45) Baumann, J.; Baitalow, F.; Wolf, G. Thermal Decomposition of Polymeric Aminoborane $(H_2BNH_2)_x$ under Hydrogen Release. *Thermochim. Acta* **2005**, *430*, 9−14.
(46) Chatterjee, T.; Thynell, S. T. Development of a Reaction Mechanism for Liquid-Phase Decomposition of Ammonia Borane. *Thermochim. Acta* **2019**, *682*, 178427.
(47) McHale, E. T.; von Elbe, G. The Deflagration of Solid Propellant Oxidizers. *Combust. Sci. Technol.* **1970**, *2*, 227−237.
(48) Zhou, W.; DeLisio, J. B.; Wang, X.; Zachariah, M. R. Reaction Mechanisms of Potassium Oxysalts Based Energetic Composites. *Combust. Flame* **2017**, *177*, 1−9.
(49) Wang, H.; Rehwoldt, M. C.; Wang, X.; Yang, Y.; Zachariah, M. R. On the Promotion of High Temperature AP Decomposition with Silica Mesoparticles. *Combust. Flame* **2019**, *200*, 296−302.
(50) Jacob, R. J.; Wei, B.; Zachariah, M. R. Quantifying the Enhanced Combustion Characteristics of Electrospray Assembled Aluminum Mesoparticles. *Combust. Flame* **2016**, *167*, 472−480.
(51) Nazir, N.; Ahanger, M. S.; Akbar, A. Micellization of Cationic Surfactant Cetyltrimethylammonium Bromide in Mixed Water-Alcohol Media. *J. Dispersion Sci. Technol.* **2009**, *30*, 51−55.
(52) Jian, G.; Zhou, L.; Piekiel, N. W.; Zachariah, M. R. Low Effective Activation Energies for Oxygen Release from Metal Oxides: Evidence for Mass-Transfer Limits at High Heating Rates. *ChemPhysChem* **2014**, *15*, 1666−1672.
(53) DeLisio, J. B.; Huang, C.; Jian, G.; Zachariah, M. R.; Young, G. Ignition and Reaction Analysis of High Loading Nano-Al/Fluoropolymer Energetic Composite Films. *52nd Aerospace Sciences Meeting*, National Harbor, Maryland, January 1−8, 2014; American Institute of Aeronautics and Astronautics, 2014.
(54) Zhou, W.; DeLisio, J. B.; Wang, X.; Egan, G. C.; Zachariah, M. R. Evaluating Free vs Bound Oxygen on Ignition of Nano-Aluminum Based Energetics Leads to a Critical Reaction Rate Criterion. *J. Appl. Phys.* **2015**, *118*, 114303.
(55) Holdren, S.; Tsyshevsky, R.; Fears, K.; Owrutsky, J.; Wu, T.; Wang, X.; Eichhorn, B. W.; Kuklja, M. M.; Zachariah, M. R. Adsorption and Destruction of the G-Series Nerve Agent Simulant Dimethyl Methylphosphonate on Zinc Oxide. *ACS Catal.* **2019**, *9*, 902−911.
(56) Perdew, J. P.; Burke, K.; Ernzerhof, M. Generalized Gradient Approximation Made Simple. *Phys. Rev. Lett.* **1996**, *77*, 3865.
(57) Vargas-Hernández, R. A. Bayesian Optimization for Calibrating and Selecting Hybrid-Density Functional Models. *J. Phys. Chem. A* **2020**, *124*, 4053−4061.
(58) Zarkevich, N. A.; Johnson, D. D. Nudged-Elastic Band Method with Two Climbing Images: Finding Transition States in Complex Energy Landscapes. *J. Chem. Phys.* **2015**, *142*, 024106.
(59) Jian, G.; Chowdhury, S.; Sullivan, K.; Zachariah, M. R. Nanothermite Reactions: Is Gas Phase Oxygen Generation from the Oxygen Carrier an Essential Prerequisite to Ignition? *Combust. Flame* **2013**, *160*, 432−437.
(60) Zhou, W.; Delisio, J. B.; Li, X.; Liu, L.; Zachariah, M. R. Persulfate Salt as an Oxidizer for Biocidal Energetic Nano-Thermites. *J. Mater. Chem. A* **2015**, *3*, 11838−11846.
(61) Wagh, A.; Raviprakash, Y.; Upadhyaya, V.; Kamath, S. D. Composition Dependent Structural and Optical Properties of PbF_2-TeO_2-B_2O_3-Eu_2O_3 Glasses. *Spectrochim. Acta, Part A* **2015**, *151*, 696−706.
(62) Rao, L. S.; Rao, P. V.; Sharma, M. V. N. V. D.; Veeraiah, N. J-O Parameters versus Photoluminescence Characteristics of $40Li_2O$-4 MO (MO=Nb_2O_5, MoO_3 and WO_3)-$55B_2O_3$:$1Nd_2O_3$ Glass Systems. *Optik* **2017**, *142*, 674−681.
(63) Bødker, M. S.; Mauro, J. C.; Youngman, R. E.; Smedskjaer, M. M. Statistical Mechanical Modeling of Borate Glass Structure and Topology: Prediction of Superstructural Units and Glass Transition Temperature. *J. Phys. Chem. B* **2019**, *123*, 1206−1213.
(64) Howes, A. P.; Vedishcheva, N. M.; Samoson, A.; Hanna, J. V.; Smith, M. E.; Holland, D.; Dupree, R. Boron Environments in Pyrex Glass - A High Resolution, Double-Rotation NMR and Thermodynamic Modelling Study. *Phys. Chem. Chem. Phys.* **2011**, *13*, 11919−11928.
(65) Kondrat'Ev, Y. V.; Butlak, A. V.; Kazakov, I. V.; Timoshkin, A. Y. Sublimation and Thermal Decomposition of Ammonia Borane: Competitive Processes Controlled by Pressure. *Thermochim. Acta* **2015**, *662*, 64−71.
(66) Lindman, N.; Simonsson, D. On the Application of the Shrinking Core Model to Liquid-Solid Reactions. *Chem. Eng. Sci.* **1979**, *34*, 31−35.

https://doi.org/10.1021/acs.jpcc.1c08985
J. Phys. Chem. C 2022, 126, 48−57